Nonlinear Dynamics manuscript No.
(will be inserted by the editor)

Supplementary Material

A broadbanded pressure differential wave energy converter based on dielectric elastomer generators

Michele Righi · Giacomo Moretti · David Forehand · Lorenzo Agostini · Rocco Vertechy · Marco Fontana

Received: date / Accepted: date

S1 Wave hydrodynamic model

This section extends the derivation of the hydrodynamic sub-model employed to represent the wave-induced pressure introduced in Eq. (18).

Sea waves are represented using linear wave theory (also referred as Stokes first order theory or Airy wave theory), which is a well-established formalism for describing ocean waves [1–3]. The theory relies on the following hypotheses: only non-breaking waves are represented; the wave amplitude is small compared to the wave length and water depth; the water flow is considered incompressible and irrotational, i.e. potential flow [1]. As a consequence, a potential ϕ, generally dependent on position and time, can be defined so that the wave-induced pressure is expressed as:

$$p_w = -\rho \frac{\partial \phi}{\partial \tau}, \tag{S1}$$

where τ represents time. The wave pressure contribution, which combines with the atmospheric and hydrostatic pressures, is caused by the acceleration of the water particles. The potential ϕ, according to [4], can be further split into three different terms:

$$\phi = \phi_o + \phi_d + \phi_r, \tag{S2}$$

where ϕ_o represents the undisturbed incident wave field (in the absence of the WEC), often referred to as the Froude-Krylov potential; ϕ_d represents the diffraction generated when the incident wave field hits a fixed object (the WEC body); and ϕ_r is the radiation term, which represents the wave field that is only due to the motion of the body.

Michele Righi
TeCIP Institute, Scuola Superiore Sant'Anna, Pisa, Italy
E-mail: righi.michele23@gmail.com

Giacomo Moretti
TeCIP Institute, Scuola Superiore Sant'Anna, Pisa, Italy

David Forehand
Institute for Energy Systems, University of Edinburgh, UK

Lorenzo Agostini
Department of Industrial Engineering, University of Bologna, Italy

Rocco Vertechy
Department of Industrial Engineering, University of Bologna, Italy

Marco Fontana
TeCIP Institute, Scuola Superiore Sant'Anna, Pisa, Italy
E-mail: marco.fontana@santannapisa.it

The Froude-Krylov and diffraction contributions are usually combined in the so-called excitation potential, $\phi_e = \phi_o + \phi_d$. Since the device dimensions are expected to be small compared to the wavelength, the diffraction contribution can be neglected ($\phi_d = 0$), as suggested in [5]. Therefore, the wave-induced pressure takes the form of Eq. (18), which is reported here for convenience:

$$p_w = -\rho\left(\frac{\partial\phi_o}{\partial\tau} + \frac{\partial\phi_r}{\partial\tau}\right) = p_o + p_r = p_e + p_r. \tag{S3}$$

The forms of the excitation and radiation contribution are detailed in Section S1.1 and Section S1.2, respectively.

S1.1 Wave excitation potential

From linear wave theory, the differentiation of a potential function ϕ_o for an undisturbed monochromatic wave field leads to the following expression:

$$p_o = \frac{\rho g H}{2}\frac{\cosh(k_w(h_d+\zeta))}{\cosh(k_w h_d)}\cos(k_w\xi - \omega\tau). \tag{S4}$$

The above relation represents the wave-induced pressure due to an undisturbed long-crested sinusoidal wave of height H, angular frequency ω and travelling in the ξ direction. ζ represents the vertical coordinate. The wave number k_w is related to the water depth h_d and to the wave frequency by the wave dispersion relationship [3]:

$$\omega^2 = g k_w \tanh(k_w h_d). \tag{S5}$$

The set of points belonging to the inlet section S_i of the control volume (see Fig. 2) can be conveniently expressed in planar polar coordinates as:

$$\mathcal{S} = \{(r,\theta,\zeta) : 0 \le r \le r_i \ \wedge\ 0 \le \theta \le 2\pi \ \wedge\ \zeta = -h_i\}. \tag{S6}$$

Since diffraction effects are neglected, averaging the undisturbed wave pressure p_o over the domain $\mathcal{S}$ leads to the excitation pressure expressed by Eq. (19):

$$p_e = \frac{1}{S_i}\iint_{\mathcal{S}} p_o \,\mathrm{d}\mathcal{S} = \frac{H}{2}\Gamma(\omega)\cos(\omega\tau), \tag{S7}$$

where $\Gamma(\omega)$ is the frequency-dependent excitation coefficient:

$$\Gamma(\omega) = \frac{\rho g}{\pi r_i^2}\frac{\cosh(k_w(h_d-h_i))}{\cosh(k_w h_d)} \int_0^{2\pi}\int_0^{r_i} r\cos(k_w r\cos\theta)\,\mathrm{d}r\,\mathrm{d}\theta \tag{S8}$$

The excitation pressure of panchromatic sea states $p_{e,p}$ is a superposition of monochromatic waves of height H_j and frequency ω_j, distributed according to a spectral model [6]:

$$p_{e,p} = \sum_j \frac{H_j}{2}\Gamma(\omega_j)\cos(\omega_j\tau + \varphi_j), \tag{S9}$$

where φ_j denotes the random phase of the different harmonic components.

S1.2 Wave radiation potential

The contribution of the radiated wave field is modelled through Eqs. (21-22), which are reproduced here:

$$p_r = -M_{ad,\infty}\ddot{\Omega}_c - \int_0^\tau k(\tau-t)\dot{\Omega}_c(t)\,\mathrm{d}t\,, \tag{S10}$$

$$\mathcal{K}(\omega) = B_r(\omega) + i\omega\big(M_{ad}(\omega) - M_{ad,\infty}\big). \tag{S11}$$

The convolution kernel $k(\tau)$ is called the retardation function, and $\mathcal{K}(\omega)$ is its frequency-domain representation. $M_{ad,\infty}$ is the infinite-frequency added mass, which adds on to the inertia of the control volume M_h of Eq. (4). It represents the inertia of the water displaced outside the control volume at the highest frequencies. $M_{ad}(\omega)$ is the frequency-dependent added mass that asymptotically tends to $M_{ad,\infty}$ at the highest frequencies. $B_r(\omega)$ is the radiation damping, which accounts

for the energy dissipation of the wave field caused by the motion of the body.

During the numerical solution procedure of the equilibrium equation (14), the convolution integral in Eq. (21) is usually approximated with a linear state-space model to reduce the computational effort [7].

S1.3 Hydrodynamic coefficients comparison

In the modelling approach presented in the paper, the coefficients $M_{ad}(\omega)$, $M_{ad,\infty}$ and $B_r(\omega)$ representing the kernel function are computed exploiting approximated analytical relations available in the literature. This approach is simple, fast and does not require the use of any additional numerical software. In the following, an alternative method to compute the hydrodynamic coefficients, based on the Boundary Element Method (BEM) is presented.

The commercial software employed for the numerical computation of the hydrodynamic coefficients is WAMIT®, a frequency-domain radiation/diffraction code that uses potential flow theory to solve for the wave field around fixed and floating bodies. Although some BEM software only provides the six traditional ship DoFs, WAMIT also allows the definition of generalized DoFs, which is crucial to model deformable bodies [8]. In this perspective, a generalized coordinate q, which describes the membrane motion, is introduced and defined by the following procedure: two static membrane configurations are identified and referred to as the "reference equilibrium configuration" and the "reference displaced configuration", to which the values of $q = 0$ and $q = 1$ are associated, respectively. A "reference displacement function" is then defined as the point-by-point difference between the reference displaced configuration and the reference equilibrium configuration. It is then assumed that any generic configuration of the membrane can be achieved through a displacement that is q times the reference displacement function from the reference equilibrium configuration. The shapes obtained from the reference equilibrium configuration by applying q times the reference displacement function do not exactly overlap the actual deformed static shapes. Nonetheless, each actual static shape (and, hence, the corresponding value of Ω_c) can be associated with a value of q, e.g., using a least-squares procedure.

The generalized coordinate q is defined in WAMIT by providing the reference and deformed equilibrium configurations. The linearized hydrodynamic coefficients are then evaluated in correspondence to the reference equilibrium configuration, i.e. at $q = 0$. An example of a surface mesh of the submerged geometry for BEM application is shown in Fig. S1.

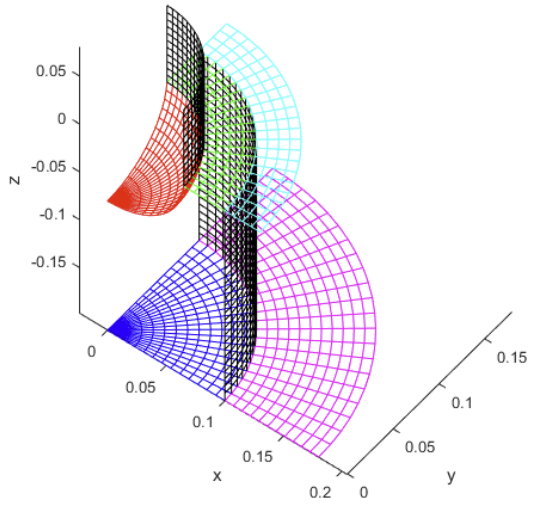

Fig. S1: WAMIT mesh employed in the calculation of the hydrodynamic coefficients. Only one quarter of the geometry is panelled because WAMIT can exploit the symmetries of the model.

WAMIT calculates the excitation coefficient $\Gamma_q(\omega)$, the added mass $M_q(\omega)$ and the radiation damping $B_q(\omega)$ as a function of the wave excitation frequency ω, as well as the asymptotic value of the frequency-dependent added mass, namely $M_{q,\infty}$. The subscript q indicates that the coefficients are computed with respect to the generalized coordinate q.

In order to compare the two sets of hydrodynamic coefficients derived from the analytical and numerical approaches, both sets have to be expressed with respect to the same coordinate set. This can be achieved through the function $q(\Omega_c)$, which relates the generalized coordinate q to the cap volume Ω_c. The two sets of coefficients (Γ, M_{ad}, B_r) and (Γ_q, M_q, B_q) are related by the following functions:

$$\begin{aligned} \Gamma(\omega) &= \Gamma_q(\omega) \left| \frac{\mathrm{d}q}{\mathrm{d}\Omega_c} \right|_{q=0}, \\ M_{ad}(\omega) &= M_q(\omega) \left(\frac{\mathrm{d}q}{\mathrm{d}\Omega_c} \Big|_{q=0} \right)^2, \\ B_r(\omega) &= B_q(\omega) \left(\frac{\mathrm{d}q}{\mathrm{d}\Omega_c} \Big|_{q=0} \right)^2. \end{aligned} \tag{S12}$$

Fig. S2 shows the trend of the analytical coefficients and those obtained from WAMIT, with respect to the wave excitation frequency.

The coefficients Γ and Γ_q coincide at both ends of the frequency range. In the static case, when $f \to 0$, the excitation coefficients tend to the product ρg, see Eq. (S8). On the other hand, at the highest frequencies, the coefficients tend to zero. In the intermediate frequency range the coefficient Γ is smaller that Γ_q, as expected. This is because the diffraction contribution ϕ_d has been neglected in the analytical formulation.
The radiation damping B_r depends quadratically on the excitation coefficient Γ, see Eq. (23). As a consequence, the difference between B_r and B_q in the intermediate frequency range is more relevant than that of

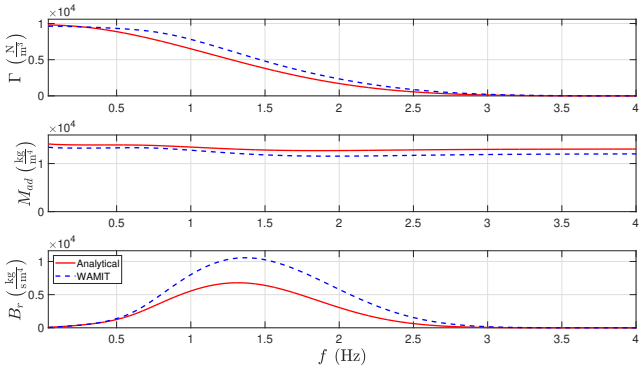

Fig. S2: Comparison of the hydrodynamic coefficients derived from the analytical relations proposed in Section 3.1 and those obtained from WAMIT simulation. From top to bottom the figure shows the excitation coefficient, the inertia of the system and the radiation damping, respectively. Note that M_{ad} represents the total inertia of the system, i.e. the constant mass in the reference equilibrium configuration plus the frequency-dependent contribution.

the excitation coefficients, see bottom plot of Fig. S2. Nevertheless, the error introduced in the system by the difference between B_r and B_q is limited by the reduced influence of the radiation contribution in the equation of motion (14).
From the centre plot of Fig. S2 it is possible to appreciate how the analytical added mass is always greater than the WAMIT result. This is in contrast with the assumption (employed in the paper) of neglecting the water velocity field of the volume cap with respect to the centre of mass of the cap itself, which should always lead to underestimating the analytical frequency-dependent added mass. Besides, since the difference between the two curves M_{ad} and M_q is almost constant, it can be concluded that the assumed infinite frequency added mass in the analytical case slightly overestimates the WAMIT result.

S2 CD-DEG model

This section describes more details on the derivation of the equilibrium equations, the initial conditions and the solution procedure for the electro-elastic model of the circular diaphragm dielectric elastomer generator (CD-DEG).

S2.1 Equilibrium equations

The CD-DEG static equilibrium equations are derived following the Euler-Lagrange approach [9]. The deformation of the CD-DEG can be described by two functions in polar cylindrical coordinates $(r(R), z(R))$, which represent the position of a material particle of the membrane in the deformed configuration. The independent variable R is the distance of a point from the axis in the reference configuration (see Fig. 3). Calling Ω_{cd} the volume of the dielectric material and $\mathbf{q} = (r(R), z(R))$, the functional to minimize is as follows:

$$\begin{aligned}\mathcal{S}(\mathbf{q}) &= \int_{\Omega_{cd}} \mathcal{L}(R, \mathbf{q}, \mathbf{q}')\, \mathrm{d}\Omega \\ &= \int_{\Omega_{cd}} (\mathcal{E}_m + \mathcal{E}_e - \mathcal{W}_p - \mathcal{W}_e)\, \mathrm{d}\Omega\,,\end{aligned} \tag{S13}$$

where the prime symbol denotes differentiation with respect to R. $\mathcal{E}_m$ and $\mathcal{E}_e$ are the elastic and electrostatic energy of the CD-DEG, respectively. $\mathcal{W}_p$ is the work done by the hydrostatic pressure on the membrane and $\mathcal{W}_e$ is the electric work done by the external power supply on the CD-DEG. The last term is non-zero only when current flows between the CD-DEG and the external conditioning electronics. The potential gravitational energy contribution of the dielectric material is neglected.

Elaborating the different energy terms, Eq. (S13) becomes:

$$\mathcal{S} = \int_0^{e_0} \left(2\pi R t_0 \left(\Psi(\lambda_1, \lambda_2) - \frac{1}{2}\epsilon E_L^2 \lambda_1^2 \lambda_2^2 \right) - \pi r^2 z' p_h \right) \mathrm{d}R\,, \tag{S14}$$

where Ψ is a volumetric strain energy density function representing the elastic energy stored by the material. Ψ can be expressed as a function of two principal stretches exploiting the material incompressibility [10]. $E_L = N_l V / t_0$ is the Lagrangian electric field, i.e. the electric field expressed in the reference configuration. p_h is the hydrostatic pressure expressed by Eq. (28), and e_0 and t_0 are the CD-DEG radius and thickness in the undeformed configuration, respectively. ϵ is the electric permittivity of the material, which is assumed constant. The dependency of the electrical properties of elastomers on the deformation is a well-known phenomenon addressed in the literature [11, 12]. Nevertheless, it has been shown that the electric permittivity of the Theraband rubber considered in this study is rather independent of deformation [13].

Defining a total energy density function per unit volume [14]:

$$\Phi(\lambda_1, \lambda_2, E_L) = \Psi(\lambda_1, \lambda_2) - \frac{1}{2}\epsilon E_L^2 \lambda_1^2 \lambda_2^2, \tag{S15}$$

the Lagrangian function $\mathcal{L}$ becomes:

$$\mathcal{L}(R, \mathbf{q}, \mathbf{q}') = 2\pi R t_0 \Phi(\lambda_1, \lambda_2, E_L) - \pi r^2 z' p_h. \tag{S16}$$

The equilibrium equations provided by the Euler–Lagrange equation (S14) read as:

$$\frac{\partial L}{\partial r} - \frac{\mathrm{d}}{\mathrm{d}R}\left(\frac{\partial L}{\partial r'}\right) = 0, \quad \frac{\partial L}{\partial z} - \frac{\mathrm{d}}{\mathrm{d}R}\left(\frac{\partial L}{\partial z'}\right) = 0. \tag{S17}$$

From the equilibrium equations (S17), the Lagrangian function (S16) and the principal stretches given in (27), which are reported here for convenience:

$$\lambda_1 = \sqrt{r'^2 + z'^2}, \quad \lambda_2 = \frac{r}{R}, \tag{S18}$$

it is possible to derive the following equilibrium equations:

$$\begin{aligned} &\frac{\tau_2 z'}{r\lambda_1} + \frac{\tau_1}{\lambda_1^3}\left(r'z'' + r''z'\right) = \frac{\lambda_1\lambda_2}{t_0}p_h, \\ &r\left(h\tau_1\right)' + t_i r'\left(\tau_1 - \tau_2\right) = 0, \end{aligned} \tag{S19}$$

where τ_1 and τ_2 are the total Cauchy principal stresses given by $\tau_1 = \lambda_1\,\partial\Phi/\partial\lambda_1$, $\tau_2 = \lambda_2\,\partial\Phi/\partial\lambda_2$, and t_i is the CD-DEG deformed thickness at a material point R. Exploiting the following geometric relations (see Fig. 3b):

$$r' = \lambda_1\sin\theta, \quad z' = \lambda_1\cos\theta, \tag{S20}$$

it is possible to convert the two second-order differential equations (S19) into the following system of four first-order differential equations:

$$\begin{aligned} \frac{\mathrm{d}\lambda_1}{\mathrm{d}R} &= \frac{\Phi_2 - \lambda_1\Phi_{12}}{R\Phi_{11}}\sin\theta - \frac{\Phi_1 - \lambda_2\Phi_{12}}{R\Phi_{11}}, \\ \frac{\mathrm{d}\lambda_2}{\mathrm{d}R} &= \frac{\lambda_1\sin\theta - \lambda_2}{R}, \\ \frac{\mathrm{d}\theta}{\mathrm{d}R} &= \frac{\Phi_2}{R\Phi_1}\cos\theta - \frac{\lambda_1\lambda_2}{t_0\Psi_1}p_h, \\ \frac{\mathrm{d}z}{\mathrm{d}R} &= \lambda_1\cos\theta, \end{aligned} \tag{S21}$$

where $\Phi_i = \partial\Phi/\partial\lambda_i$ and $\Phi_{ij} = \partial^2\Phi/\partial\lambda_i\partial\lambda_j$. Note that imposing $E_L = 0$, (S21) resorts to system (29).

Eq. $(S21)_4$ is exactly Eq. $(S20)_2$, while Eq. $(S21)_2$ is obtained by differentiating Eq. $(S18)_2$ with respect to R and using Eq. $(S20)_1$. With simple algebraic computation it is possible to show that $r'z'' - r''z' = -\lambda_1\theta'$, so that Eq. $(S21)_3$ is obtained from Eq. $(S19)_1$. Lastly, combining Eq. $(S19)_2$ and Eq. $(S21)_2$ yields, after simplification, Eq. $(S21)_1$.

S2.2 Boundary/initial conditions

The boundary conditions of the problem (S21) are as follows:

$$\begin{aligned} \lambda_1(0) - \lambda_2(0) &= 0, \\ \lambda_2(e_0) &= \lambda_p, \\ \theta(0) &= \pi/2, \\ z(0) &= 0. \end{aligned} \tag{S22}$$

All the conditions are applied at $R = 0$, except for Eq. $(S22)_2$, which holds at $R = e_0$. The system (S21) with the conditions (S22) is thus a boundary-value problem.

A shooting method procedure can be conveniently employed to solve the system, making use of four initial conditions at $R = 0$ (instead of a set of mixed boundary conditions at $R = 0$ and $R = e_0$). With this approach, the equilibrium equations are integrated from the axial symmetry axis ($R = 0$) towards the exterior. Nonetheless, since the system of equations (S21) is singular at $R = 0$, the integration is performed from $R = \delta$, with δ a sufficiently small constant.

A Taylor series expansion of $\lambda_1(0)$, $\lambda_2(0)$, $\theta(0)$ and $z(0)$ is employed to estimate the value of the unknown functions at $R = \delta$:

$$\begin{aligned} \lambda_1(\delta) &= \lambda_0 + \frac{1}{2}\lambda_1''(0)\delta^2 + \mathcal{O}(\delta^4), \\ \lambda_2(\delta) &= \lambda_0 + \frac{1}{2}\lambda_2''(0)\delta^2 + \mathcal{O}(\delta^4), \\ \theta(\delta) &= \frac{\pi}{2} + \theta'(0)\delta + \mathcal{O}(\delta^3), \\ z(\delta) &= \frac{1}{2}z''(0)\delta^2 + \mathcal{O}(\delta^4). \end{aligned} \tag{S23}$$

Note that, placing the origin of coordinate system $r - z$ on the membrane tip (see Fig. 3) provides $z(0) = 0$ in Eq. $(S22)_4$ and Eq. $(S23)_4$. Without that choice there would have been a further unknown to solve for (i.e., $z(0)$ itself), considerably increasing the complexity of the solution procedure.

Differentiating the first two equations of the system (S21) with respect to R yields two equations in λ_1'' and λ_2'', the solution of which, evaluated at $R=0$, reads as:

$$\begin{aligned}\lambda_1''(0) &= -\frac{\lambda_2\Phi_{22} - 3\lambda_2\Phi_{12} + 3\Phi_2}{8\Phi_{22}}\theta'(0)^2,\\ \lambda_2''(0) &= -\frac{\lambda_2\Phi_{22} - \lambda_2\Phi_{12} + \Phi_2}{8\Phi_{22}}\theta'(0)^2.\end{aligned} \tag{S24}$$

The value of $\theta'(0)$ can be determined by evaluating Eq. $(\text{S21})_3$ at $R=0$:

$$\theta'(0) = -\frac{\lambda_1(0)^2 p_h(0)}{2t_0\Phi_1} = -\frac{\rho g z_t \lambda_0^2}{2t_0\Phi_1}, \tag{S25}$$

while $z''(0)$ can be obtained by differentiating Eq. $(\text{S21})_4$ and then evaluating at $R=0$:

$$z''(0) = -\lambda_1(0)\theta'(0) = \frac{\rho g z_t \lambda_0^3}{2t_0\Phi_1}. \tag{S26}$$

S2.3 Solution procedure

The following procedure has been employed to solve the system of equations (S21) with initial conditions (S23):

1. The stretch λ_0 at the pole of the CD-DEG, and the level of electric activation E_L are chosen and replaced in the equilibrium equations (S21) and in the initial conditions (S23);
2. The system (S21) is integrated treating z_t as a parameter (the available `ParametricNDSolveValue` solver of the commercial software Wolfram Mathematica® has been employed);
3. The parametrized solution of the functions λ_1, λ_2, θ and z obtained in the previous step are employed to write the constraint equation $\lambda_2(e_0) = \lambda_p$ (see Eq. $(\text{S22})_2$), whose solution yields the value of z_t that satisfies the system (S21) with the imposed values of λ_0 and E_L;
4. The corresponding value of the water head h_0 (see Fig. 3b) is then computed as $h_0 = z_t - z(e_0)$;
5. By repeating steps (1) to (4) for different values of λ_0 and E_L, the maps of the following quantities are derived: $h_0(\lambda_0, E_L)$, $\Omega_c(\lambda_0, E_L)$, $\zeta_c(\lambda_0, E_L)$, $\mathcal{E}_m(\lambda_0, E_L)$ and $C(\lambda_0, E_L)$.

The values of the volume, elastic energy and capacitance are computed from the knowledge of the CD-DEG deformed shapes as follows:

$$\begin{aligned}\Omega_c &= \pi\int_0^{e_0} \lambda_1\lambda_2^2 R^2\cos\theta\,\mathrm{d}R,\\ \mathcal{E}_m &= 2\pi t_0\int_0^{e_0} R\Psi\,\mathrm{d}R,\\ C &= \epsilon\int_S \frac{1}{t_i}\,\mathrm{d}S = \frac{2\pi\epsilon}{t_0}\int_0^{e_0} R\lambda_1^2\lambda_2^2\,\mathrm{d}R,\end{aligned} \tag{S27}$$

where ϵ is the permittivity of the material and S is the surface of the CD-DEG in the deformed configuration.

The computation of the centre of mass of the CD-DEG cap ζ_c requires special attention since the coordinate reference system employed in the CD-DEG submodel does not coincide with that used to derive the equation of motion (14). In particular, the former is mobile while the latter is fixed. Based on Fig. 3, the following relation holds:

$$\zeta_c = -\left(h_0 + \hat{\zeta}_c\right), \tag{S28}$$

where both h_0 and $\hat{\zeta}_c$ are treated as positive quantities. From the solution procedure h_0 is computed as $h_0 = z_t - z(e_0)$, while $\hat{\zeta}_c$ is calculated as follows:

$$\hat{\zeta}_c = z(e_0) - \frac{\pi}{\Omega_c}\int_0^{e_0} \lambda_1\lambda_2^2 R^2 z\cos\theta\,\mathrm{d}R. \tag{S29}$$

A root-finding algorithm is necessary to solve the non-linear constraint equation $(\lambda_2(e_0) - \lambda_p = 0)$ of step (3) of the solution procedure. A good practice is to start the mapping procedure from a value of λ_0 slightly higher than the value of the pre-stretch λ_p, so that a reliable starting point for the root-finding iteration is a value of z_t slightly higher than zero. The procedure is

then repeated for increasing values of λ_0, and the solution for z_t at the previous step is used as a first guess for the current iteration.

This solution process is fast and reliable and it requires only a few seconds of computational time on a standard laptop to provide a complete electro-mechanical characterization of the CD-DEG. The main advantage is that just one root-finding procedure is required for every couple of imposed values (λ_0, E_L). Conversely, in a standard shooting method algorithm, an iterative solution procedure is required (for non-linear systems) until the guessed initial condition satisfies the boundary condition of the corresponding boundary value problem [15].

S2.4 Comparison of models

The approach presented in the previous sections provides the exact solution of the CD-DEG hydro-electro-elastic fully-coupled problem in static conditions. In the paper, in contrast, we employed a single-DoF model, in which the electrical and mechanical CD-DEG responses are partly decoupled: the shapes of the CD-DEG are mapped making reference to static electrically-inactive conditions, and the electro-elastic interaction is then accounted for through the following equilibrium equation (which is the equivalent to Eq. (14) in static conditions):

$$\rho g \zeta_c' \Omega_c + \rho g \zeta_c + p_{a,r} + \mathcal{E}_m' - \frac{C'}{2} V^2 = 0, \tag{S30}$$

According to this approach, a set of approximate CD-DEG shapes and the corresponding values of $\mathcal{E}_m$, C and ζ_c are first identified, by imposing $V = 0$ in Eq. (S30) (which is equivalent to imposing $E_L = 0$ in Eqs. (S21)). Then, the effect of electric activation is accounted for by the term $0.5C'V^2$, so that changing the applied voltage modifies the equilibrium position of the CD-DEG through a change in Ω_c, which in turn changes the elastic energy $\mathcal{E}_m(\Omega_c)$. With this approximation, and in contrast with the solution of Eqs. (S21), the set of possible deformed shapes obtained by varying the electric activation is the same as that obtained by changing the differential pressure on the CD-DEG.

The comparison of the two solutions (fully-coupled vs. 1-DoF partially-coupled) is carried out considering the dielectric material and the PD-WEC geometric features presented in the paper, which are reported in Table S1 for convenience.

Material	Theraband Rubber
Hyperelastic model	Gent-Gent
Gent-Gent parameters	$\mu = 132\,\text{kPa}$,
	$J_m = 45$,
	$C_2 = 10\,\text{kPa}$
Radius	$e = 65\,\text{mm}$
Thickness	$t_0 = 0.22\,\text{mm}$
Pre-stretch	$\lambda_p = 1.6$
Number of layers	$N_l = 1$
Relative dielectric constant	$\epsilon_r = 2.7$

Table S1: PD-WEC features.

S2.4.1 Load-deformation

The same values of the stretch λ_0 at the membrane tip and electric activation $\tilde{E}_L$ are imposed to both the fully-coupled and 1-DoF partially-coupled models, and the water column height h_0, which is derived from the system equilibrium, is compared. For the aim of the CD-DEG model comparison, the air chamber pressure $p_{a,r}$ has been set equal to zero, and the level of electric activation has been expressed in terms of the non-

dimensional Lagrangian electric field:

$$\tilde{E}_L = \frac{E_L}{\sqrt{\mu/\epsilon}}. \tag{S31}$$

The map for $h_0^*(\lambda_0, \tilde{E}_L)$ for the fully-coupled method is directly obtained from the solution procedure of Section S2.3. For the partially-coupled method, the function $h_0(\lambda_0, \tilde{E}_L)$ can be derived from Eq. (S30) as follows:

$$h_0(\lambda_0, \tilde{E}_L) = -\left(\hat{\zeta}_c'\Omega_c + \hat{\zeta}_c\right) + \frac{1}{\rho g}\left(\mathcal{E}_m' - \frac{1}{2}\frac{\mu}{\epsilon}t_0^2\tilde{E}_L^2 C'\right). \tag{S32}$$

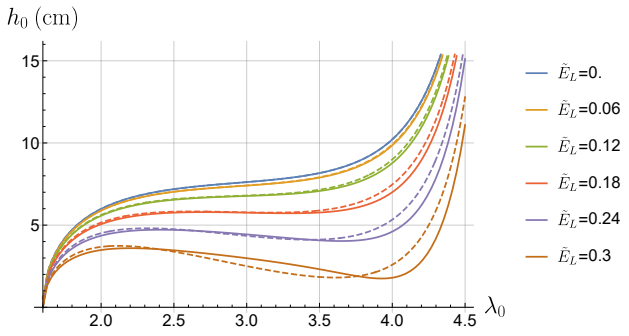

Fig. S3: CD-DEG static load-deformation characteristics. The horizontal axis represents the stretch at the tip of the membrane and the vertical axis represents the water column height above the plane housing the membrane perimeter. Solid lines are the solutions of the fully-coupled method, see Eqs. (S21). Dashed lines represent the solutions of the 1-DoF partially-coupled formulation, see Eq. (S32). The non-dimensional Lagrangian electric field $\tilde{E}_L$ increases linearly from top to bottom.

The static load-deformation characteristics for the two solution methods are represented in Fig. S3. Each of the curves in the figure refers to a constant value of $\tilde{E}_L$. Since $\tilde{E}_L$ is, by definition, proportional to the voltage V and a set of constant parameters, each curve represents the iso-potential response of the system at different levels of electrical load. The fully-coupled and 1-DoF partially-coupled models are identical in the purely mechanical scenario, indeed they provide the same solution (top curve of Fig. S3). The difference between the two sets of solutions increases with the electric activation $\tilde{E}_L$.

We define an average relative difference function $\Delta e(\tilde{E}_L)$ as follows: for each value of $\tilde{E}_L$, the point-by-point relative difference (with respect to the fully-coupled solution) is computed for every value of λ_0, then the average integral value with respect to λ_0 is computed. The trend of the function $\Delta e(\tilde{E}_L)$ is represented in Fig. S4, which shows that the difference between the fully-coupled and the 1-DoF partially-coupled solution increases with $\tilde{E}_L$.

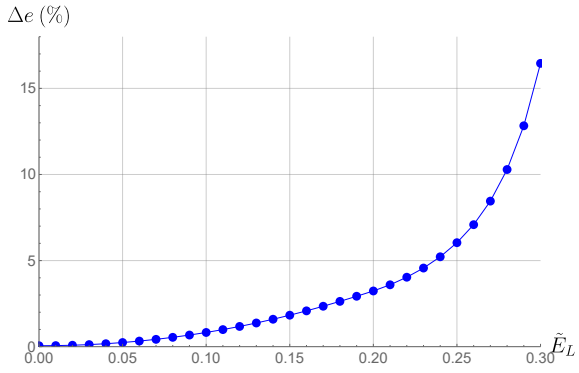

Fig. S4: Percentage difference (with respect to the fully-coupled solution) between the 1-DoF partially-coupled solution and the fully-coupled solution as a function of the non-dimensional Lagrangian electric field $\tilde{E}_L$.

Fig. S3 also shows that, at a given value of $\tilde{E}_L$, the difference between the fully-coupled solution and the 1-DoF partially-coupled solution increases as λ_0 increases. Since, in this plot, the Lagrangian electric field is constant for each curve, the actual electric field E

across the CD-DEG faces increases with the deformation, $E = E_L\lambda_1\lambda_2$. Therefore, the effect of the electric activation on the accuracy of the partially-coupled model becomes more relevant at high stretch levels.

The total Cauchy stresses can be written as:

$$\tau_i = \lambda_i \frac{\partial \Psi(\lambda_1, \lambda_2)}{\partial \lambda_i} - \epsilon E_L^2 \lambda_1^2 \lambda_2^2, \quad \text{for} \quad i = 1, 2. \tag{S33}$$

By way of example, holding the deformation (λ_1, λ_2) constant and increasing the electric activation $\tilde{E}_L$ eventually leads to negative values of total stress. The conditions $\tau_i > 0$ must be verified at every point of the CD-DEG and at any instant, otherwise local loss of tension can occur, which could lead to instability phenomena (e.g. membrane wrinkling) with possible failure of the system [16, 17].

The local CD-DEG condition $\tau_i > 0$ can be associated with the global requirement that $h_0(\lambda_0, \tilde{E}_L) \geq 0$. When the Maxwell stress component $\epsilon E_L^2 \lambda_1^2 \lambda_2^2$ becomes predominant with respect to the mechanical stress $\lambda_i \partial \Psi(\lambda_1, \lambda_2)/\partial \lambda_i$, the total Cauchy stresses are no longer able to sustain the water hydrostatic pressure and the system presents no stable configurations ($h_0 < 0$).

In the previous examples we made reference to loading curves with constant Lagrangian electric field $\tilde{E}_L$ for computational convenience. In practice, the real (Eulerian) electric field should be adapted to the actual CD-DEG deformation to maximize the generation of electric energy [18].

S2.4.2 Capacitance

Since the electrical power provided by the PD-WEC is proportional to the CD-DEG capacitance variation, see Eq. (17), a comparison between the CD-DEG capacitance computed from the fully-coupled solution and that obtained from the 1-DoF partially-coupled solution is presented in Fig. S5. Here, the capacitance obtained from Eq. $(S27)_3$ is plotted with respect to the water head h_0 for different values of the non-dimensional Lagrangian electric field $\tilde{E}_L$.

The maximum relative difference between the exact and approximated solutions is always less than 5%, which is an acceptable approximation considering the global accuracy of the model and the uncertainties generated by the other assumptions, especially those regarding the hydrodynamics.

Note that, although the difference in the load-displacement characteristic (Fig. S3) between the two sets of solutions rapidly grows with $\tilde{E}_L$ (see Fig. S4), the error in the capacitance remains limited.

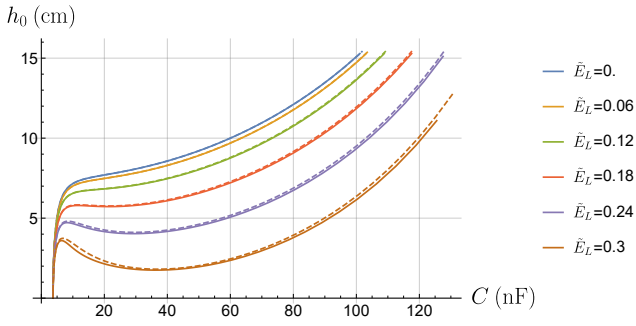

Fig. S5: CD-DEG capacitance vs. the water column height h_0. Solid lines represent the exact solutions of Eqs. (S21) and dashed lines represent the solutions provided by the energetic approach of Eq. (S32). The non-dimensional Lagrangian electric field increases from the top to the bottom curves.

Note that some of the curves in Fig. S5, similarly to those in Fig. S3, present a portion with negative slope. In those regions, the membrane would be prone to electro-mechanical instability (referred to as snap-through instability [10] or pull-in instability [16, 17]) in

the presence of a constant applied electrical potential. In practice, this effect can be mitigated/removed by choosing an appropriate electrical driving strategy for the DEG [19].

References

[1] McCormick, Michael E. *Ocean engineering wave mechanics*. John Wiley & Sons, 1973.

[2] Falnes, Johannes. *Ocean waves and oscillating systems: linear interactions including wave-energy extraction*. Cambridge university press, 2002.

[3] Andersen, Thomas Lykke, Frigaard, Peter, and Burcharth, Hans F. "Water Wave Mechanics". In: *Lecture Notes. Department of Civil Engineering, Aalbrorg University* (2007).

[4] Alves, Marco. "Numerical simulation of the dynamics of point absorber wave energy converters using frequency and time domain approaches". In: *UNIVERSIDADE TECNICA DE LISBOA-INSTITUTO SUPERIOR TECNICO* (2012).

[5] Viuff, Thomas Hansen, Andersen, Morten Thøtt, Kramer, Morten, and Jakobsen, Morten Møller. "Excitation forces on point absorbers exposed to high order non-linear waves". In: *European Wave and Tidal Energy ConferenceEuropean Wave and Tidal Energy Conference*. Technical Committee of the European Wave and Tidal Energy Conference. 2013.

[6] Moretti, Giacomo, Rosati Papini, Gastone Pietro, Daniele, Luca, Forehand, David, Ingram, David, Vertechy, Rocco, and Fontana, Marco. "Modelling and testing of a wave energy converter based on dielectric elastomer generators". In: *Proceedings of the Royal Society A* 475.2222 (2019), p. 20180566.

[7] Yu, Z and Falnes, J. "State-space modelling of a vertical cylinder in heave". In: *Applied Ocean Research* 17.5 (1995), pp. 265–275.

[8] Lee, Chang-Ho and Newman, J Nicholas. "WAMIT User manual". In: *WAMIT, Inc* (2006).

[9] Goldstein, Herbert, Poole, Charles, and Safko, John. *Classical mechanics*. AAPT, 2002.

[10] Holzapfel, Gerhard A. "Nonlinear solid mechanics: a continuum approach for engineering science". In: *Meccanica* 37.4 (2002), pp. 489–490.

[11] Tröls, Andreas, Kogler, Alexander, Baumgartner, Richard, Kaltseis, Rainer, Keplinger, Christoph, Schwödiauer, Reinhard, Graz, Ingrid, and Bauer, Siegfried. "Stretch dependence of the electrical breakdown strength and dielectric constant of dielectric elastomers". In: *Smart Materials and Structures* 22.10 (2013), p. 104012.

[12] Jiang, Liang, Betts, Anthony, Kennedy, David, and Jerrams, Stephen. "Investigation into the electromechanical properties of dielectric elastomers subjected to pre-stressing". In: *Materials Science and Engineering: C* 49 (2015), pp. 754–760.

[13] Chen, Yi, Agostini, Lorenzo, Moretti, Giacomo, Fontana, Marco, and Vertechy, Rocco. "Dielectric elastomer materials for large-strain actuation and energy harvesting: a comparison between styrenic rubber, natural rubber and acrylic elastomer". In: *Smart Materials and Structures* 28.11 (2019), p. 114001.

[14] Dorfmann, Luis and Ogden, Ray W. *Nonlinear theory of electroelastic and magnetoelastic interactions*. Vol. 510. Springer, 2014.

[15] Adam, Badradeen and Hashim, Mohsin HA. "Shooting method in solving boundary value problem". In: *International Journal of Research and Reviews in Applied Sciences* 21.1 (2014), p. 8.

[16] Suo, Zhigang. "Theory of dielectric elastomers". In: *Acta Mechanica Solida Sinica* 23.6 (2010), pp. 549–578.

[17] Zurlo, Giuseppe, Destrade, Michel, DeTommasi, Domenico, and Puglisi, Giuseppe. "Catastrophic thinning of dielectric elastomers". In: *Physical review letters* 118.7 (2017), p. 078001.

[18] Papini, Gastone Pietro Rosati, Moretti, Giacomo, Vertechy, Rocco, and Fontana, Marco. "Control of an oscillating water column wave energy converter based on dielectric elastomer generator". In: *Nonlinear Dynamics* 92.2 (2018), pp. 181–202.

[19] Broderick, Hannah Conroy, Righi, Michele, Destrade, Michel, and Ogden, Ray W. "Stability analysis of charge-controlled soft dielectric plates". In: *International Journal of Engineering Science* 151 (2020), p. 103280.